Advanced Ceramics Progress: Vol. 10, No. 2, (Spring 2024) 23-31

Materials and Energy Research Center
MERC

Contents lists available at ACERP

Advanced Ceramics Progress

Journal Homepage: www.acerp.ir

Original Research Article

Corrosion Studies on the Hydroxyapatite-Gelatin-Mono Layered Graphene Oxide Nanocomposite Coating on SS316L

Hurieh Mohammadzadeh *, Robabeh Jafari

Assistant professor, Department of Materials Science and Engineering, Faculty of Engineering, Urmia University, Urmia, Iran.

* Corresponding Author Email: h.mohamadzadeh@urmia.ac.ir (Hurieh Mohammadzadeh) URL: https://www.acerp.ir/article_209820.html

ARTICLE INFO

Article History:
Received: 02 August 2024
Revised: 16 November 2024
Accepted: 02 December 2024

Keywords:
Nanocomposite,
Coating,
Single-layer Graphene Oxide/ Hydroxyapatite/ Chitosan,
Corrosion

ABSTRACT

Stainless steel 316L (SS316L) is a good candidate for metal implants due to its excellent tensile strength and high corrosion resistance. However, its surface needs to be improved to enhance biocompatibility, bioactivity, and antimicrobial functions. Among bioceramics, hydroxyapatite ($Ca_{10}(PO_4)_6(OH)_2$) is widely used in medical applications due to its mineral composition, which is similar to the natural hard tissues of the body, and its biomimetic morphology. Chitosan possesses attractive biological properties such as good biodegradability, non-toxicity, biocompatibility, and cellular bioavailability. Graphene oxide demonstrates antibacterial activity against bacteria, fungi, and viruses, which can help limit cancer-causing infections in surgeries. Accordingly, an HA-based nanocomposite (HA-CS-GO) was deposited on SS316L sheets by electrophoretic deposition. Nanoparticle HA was synthesized via the sol-gel method. The coating was applied at 80V for 1 minute. To study the products and coating, various analyses were employed, including XRD, SEM, FTIR, electrochemical impedance spectroscopy (EIS), and polarization analysis. The results confirmed the successful synthesis of HA. The nanocomposite coating (thickness ~12.7 µm) was properly deposited on SS316L. The corrosion resistance improved with the coating; the current density decreased from 7.6 to 1.4 $\mu A \cdot cm^{-2}$. The mechanism of corrosion was evaluated by EIS data. The corresponding equivalent circuit was proposed, and the dielectric capacitor and resistance values were estimated.

https://doi.org/10.30501/acp.2024.466016.1154

1. INTRODUCTION

Biomaterials, as substances engineered to interact with biological systems for medical purposes, are produced in various forms such as soft and hard tissues, scaffolds, implants, etc., and can be absorbable or non-absorbable in the body. Additionally, they may have neutral, bioactive, biostable, or biodegradable properties (Dvorsky et al., 2020; Hudecki et al., 2018). The properties that a biomaterial must possess to be used as an implant include biocompatibility, corrosion resistance, non-toxicity, excellent mechanical properties, and the absence of foreign body reactions (Eliaz, 2019). Different materials, including metallic components, polymers, ceramics, or composite materials, can be used as biomaterials. Metallic components include Ti and its alloys (Liao et al., 2022), stainless steels (Verma et al., 2023), and Mg and its alloys (Saadati et al., 2021b), which are chosen for their high mechanical properties, good corrosion resistance, and biocompatibility in physiological environments (Harun et al., 2018). Among these alloys, stainless steel is particularly effective in bone stabilization and other orthopedic, medical, and dental applications due to its excellent mechanical properties, high corrosion resistance, and affordability (Logesh et al., 2022; Wadood, 2021). Therefore, to enhance biocompatibility by increasing corrosion

Please cite this article as: Mohammadzadeh, H. & Jafari, R. (2024). Corrosion Studies on the Hydroxyapatite-Gelatin-Mono Layered Graphene Oxide Nanocomposite Coating on SS316L, *Advanced Ceramics Progress*, 10(2), 23-31. https://doi.org/10.30501/acp.2024.466016.1154

resistance, bioactive and biocompatible ceramic coatings are developed. Hydroxyapatite (HA), a synthetic bioceramic, with the chemical formula $Ca_{10}(PO_4)_6(OH)_2$ is a ceramic biomaterial (Kuo & Du, 2022) with outstanding bio-features such as biocompatiblity (Modolon et al., 2021a) and similarity to the hard tissues in the body of mammals. Due to its strong bonding with bone tissue (Baslayici et al., 2022), HA and its composites are widely used in medical applications like implants (Choi et al., 2020) because of their high surface-to-volume ratio, reactivity (Modolon et al., 2021), biomimetic morphology, and osteogenesis induction, to name a few (Asadipour et al., 2019; Das & Chakraborti, 2021). One of the common methods for HA synthesis is sol-gel (Chen et al., 2011).

Ceramics are often used in combination with natural polymers, such as chitosan, to form a uniform and non-porous structure. Among natural polymers, there is a growing interest from researchers worldwide in chitosan (CS), which is a linear and cationic polysaccharide (Zhang et al., 2022). Due to the presence of amino groups in its structure, CS possesses attractive physicochemical and biological properties such as biocompatibility, biodegradability, hydrophilicity, non-toxicity, and high cellular bioavailability. Moreover, CS has acceptable mechanical strength, good thermal stability, and can combine with metals and proteins due to its specific chemical structure (Saadati et al., 2021a).

Graphene and its derivatives have exhibited antibacterial activities against bacteria, fungi, and viruses (Zahra et al., 2023). Graphene oxide (GO) can be synthesized by chemically oxidizing graphite. GO, a unique material, is composed of a single monomolecular layer of graphite with various oxygen-containing functionalities (e.g., carbonyl, carboxyl, and hydroxyl groups) that help disperse GO in polymeric solutions and enhance its hydrophilicity (Guo et al., 2023; Nair et al., 2022). GO is a biocompatible, carbon-based material, which is efficiently used in nanocomposite materials, polymer composite materials, biomedical applications, and catalysis (Naderi & Nadri, 2022; Sahoo et al., 2023). Additionally, GO exhibits a hydrophilic nature, which is vital for biological functionality by improving cell adhesion, cell viability, and boosting cell proliferation (Staneva et al., 2021).

Several methods have been employed to deposit and form ceramic/polymeric base coatings over metal substrates, including electrochemical deposition (Perju et al., 2022), electrophoretic (EPD) (Akram et al., 2023), sputtering (Monai et al., 2023), sol-gel (Shanmugapriya et al., 2022), immersion (Khalid et al., 2013), plasma spray (Vahabzadeh et al., 2015), hot isostatic press (Onoki & Hashida, 2006), deposition pulsed laser (Dhinasekaran et al., 2021). Among these approaches, EPD has become popular for a variety of emerging applications in both academic and industrial sectors due to its simplicity, short processing time, cost-effectiveness, and ability to deposit a wide variety of materials and combinations (Sorkhi et al., 2019). Asgar et al. coated GO on titanium alloy (Ti6Al4V) by EPD and reported an improvement in corrosion resistance due to the GO coating (Asgar et al., 2019). It has been reported that GO in HA/CC/GO coatings (deposited by EPD) on AZ91D increased corrosion resistance by removing surface cracks (Askarnia et al., 2021). Shi et al. deposited GO–CS–HA nanocomposites on a Ti substrate as orthopedic-related implants via electrophoretic deposition and studied the microstructure and corrosion behavior of the coating (Shi et al., 2016). In another study, the HA-GO nanocomposite coating was applied to a Ti substrate through EPD to improve biomedical functionality (Fardi et al., 2020). It has been reported that the mechanical properties and corrosion resistance of the coating can be improved with GO (Pan et al., 2023).

Due to the importance and attractiveness of HA and GO for biological applications, numerous studies have been conducted on their composites as coatings over implant metals. However, the coating of GO in combination with HA and CS needs further study to examine the morphology, microstructure, and corrosion behavior of the coating in the body environment. Given the lack of systematic research into HA-CS-GO coatings on SS316L sheets, the current research aims to study the features of the HA-CS-GO coating in detail.

2. MATERIALS AND METHODS

2.1. MATERIALS

For the coating material, npHA was synthesized. Moreover, some chemicals were used for coating setup including the electrolyte. For this purpose, ethanol 99.9%, di-phosphorus pentoxide (P_2O_5, Ghatran-Shimi, Iran), calcium nitrate ($Ca(NO_3)_2.4H_2O$, Sigma-Aldrich), deionized water, acetic acid (CH_3COOH), chitosan, gelatin and ascorbic acid (Sigma-Aldrich), single-layer graphene oxide (GO), magnesium nitrate ($Mg(NO_3)_2.6H_2O$, Merck), and isopropyl alcohol (C_3H_8O, Sigma-Aldrich) were purchased. The SS316L sheets (Table 1) were substrates, which were sandblasted and cut into the dimensions of 20×10 mm^2.

TABLE 1. The chemical composition of SS316L sheets.

Fe	Cr	Ni	C	Mn	P	S	Si	Mo	N
Balance	17.1	12.2	0.03	2.02	0.045	0.03	0.75	2.2	0.1

2.2. SYNTHESIS OF nHA

To synthesize npHA by the sol-gel approach, the Ca/P molar ratio was set to 10:3. Then, 1.67 M of $Ca(NO_3)_2{\cdot}4H_2O$ and 0.5 M of P_2O_5 were prepared in separate beakers by dissolving them in pure ethanol for 0.5 h. The P_2O_5 solution was gradually added to the $Ca(NO_3)_2{\cdot}4H_2O$ solution and mixed for 3 h to form a gel. The gel product was heated at 60 °C for 24 h to dehumidify. The resulting powder was calcined at 650 °C for 3 h to produce the white-colored HA nanopowder.

2.3. COATING

Coating of HA-CS-GO was performed on SS316L sheets using the EPD approach. For EPD, CS (0.5 g/L), GO (0.015 g/L), Gel (5 g/L), and HA (0.5 g/L) were dispersed in the electrolyte suspension. CS and Gel were dissolved in a mixture of ethanol and deionized water (80/20 volume ratio) with 0.25 cc acetic acid and ethanol. HA nanopowder was added to this suspension. After 5 h of stirring, GO was added to the solution and mixed for an additional 1 h. An ultrasonic probe was employed to disperse the suspension for 5 min. Finally, the electrolyte was stirred for another 5 h using a magnetic stirrer. The SS316L sheets were degreased in a 10 wt.% NaOH solution at 60 °C for 0.5 h, followed by immersion in an acetone solution in an ultrasonic bath for 1 h. They were then placed in hydrochloric acid for 1 min, washed with distilled water, and dried.

For coating by EPD, a two-electrode (SS316L, 20×10 mm^2) cell was used for the substrate and anode. The distance between the electrodes was set to 1 cm. To stabilize the electrolyte, it was kept at room temperature for 3 days. Before coating, it was dispersed for 2 h. The coating process was performed at 80 V for 1 min.

2.4. ANALYSIS

The chemical analysis was performed using X-ray diffraction (XRD) with a PHILIPS XRD apparatus (PW1730, Netherlands, Cu Kα, λ=1.5418 Å, step size=0.05°, time per step=1 s). The crystallite size was determined from the XRD pattern using X'Pert-Pro software.

A scanning electron microscope (SEM, Zeiss Sigma 300 - Germany) equipped with EDS was used for the microstructural study of the synthesized powders and coating. The Fourier transform infrared (FTIR) spectra of npHA and GO were collected with an FTIR spectrophotometer (Thermo Nicolet NEXUS 670 FTIR, Thermo Scientific, USA) in absorption mode over the wavelength range of 400-4000 cm^{-1}.

Potentiodynamic polarization tests (scanning speed of 1 mV/s and voltage from -1 to 0.9 mV) and electrochemical impedance spectroscopy (EIS, frequency range from 100 kHz to 10 mHz) were employed at room temperature to study the corrosion response of the samples in simulated body fluid (SBF) using a Potentiostat/Galvanostat/Impedance Analyzer (Metrohm DropSens, μStat-I 400s). For this purpose, G3-89 1999 ASTM standards were followed, where the counter, reference, and working electrodes were a platinum (Pt) plate, a KCl-saturated calomel (Ag/AgCl) electrode, and the coated samples, respectively. The EIS data were analyzed using the equivalent circuit simulated by ZView software.

3. RESULTS AND DISCUSSION

3.2. SYNTHESIZED NANOMATERIALS

Figure 1(a) illustrates the X-Ray Diffraction (XRD) pattern of the synthesized npHA, which was in accordance with the reference code JCPDS no. 09-0432. The average crystallite size of the synthesized npHA was calculated through the Debye-Scherrer equation (Eq. 1) from five major peaks to be 24.4 nm. The parameters of this equation are D, κ, λ, β, and θ, which are representatives of the crystallite size, constant coefficient (0.94), wavelength (1.54 Å), Bragg angle width, and Bragg angle, respectively(Modolon et al., 2021b).

$$D = \frac{\kappa\lambda}{\beta\cos\theta} \quad (1)$$

Figure 1(b) shows the FTIR spectrum of the npHA product. The chemical groups OH^- and CO_3^{2-}, characteristic of nonstoichiometric HA, were found in the FTIR spectrum due to the synthesis route (Gheisari et al., 2015). There is a relatively wide absorption band at 3560 cm^{-1} showing the stretching vibration of the hydroxyl functional group (OH^-). The absorption peaks at 3440 and 2921 cm^{-1} correspond to the stretching and bending vibrations of water absorption bonds (Kesmez, 2020; Priyam et al., 2019). Two peaks at 4515 and 1460 cm^{-1} are associated with the asymmetric stretching of the CO_3^{2-} group. Accordingly, the C from organic materials is not completely decomposed and may instead dissolve in the crystal (Mujahid et al., 2015). he peaks that occurred at 1039, 972, 729, 571 cm^{-1}, and 449 cm^{-1} correspond to the asymmetric bending and stretching vibrations of the phosphate group PO_4^{3-} (Prasanna & Venkatasubbu, 2018).

Figure 1(c) illustrates the microstructure of the produced nP-HA powder. According to the SEM images and measurements by ImageJ software, HA particles were spherical with an average size of ~31.7 nm, which agglomerated to form clusters with an average diameter ranging from 210 nm to 4.1 μm.

Figure 2(a) shows the FTIR spectra of GO to study the compositions and bonding. There is a broad peak at 3439 cm^{-1}, which corresponds to the stretching vibrations of the hydroxyl (-OH) and water bonds. The absorption at 1718 cm^{-1} shows the stretching vibrations of the carbonyl group (C=O). The peak at 1620 cm^{-1} relates to C=C stretching vibrations. The peaks at 1213 and 1049 cm^{-1} correspond to C-O stretching vibrations (Jeyaseelan et al., 2021; Kusrini et al., 2020).

Figure 2(b) shows the SEM images of GO, while the corresponding molecular structure is illustrated in Figure

2(c). The SEM image in Figure 2(b) reveals that the nano-sheets of GO are very smooth. GO has a metastable nature, causing the sheets to fold at the edges. This deviation from thermodynamic stability arises from the oxygen-containing functional groups in the basal planes and sp^3 carbons, as shown in Figure 2(e) (Al-Gaashani et al., 2019). The covalence bonding between C atoms and the functional chemical groups of -OH, -O and =O is shown in Figure 2(c).

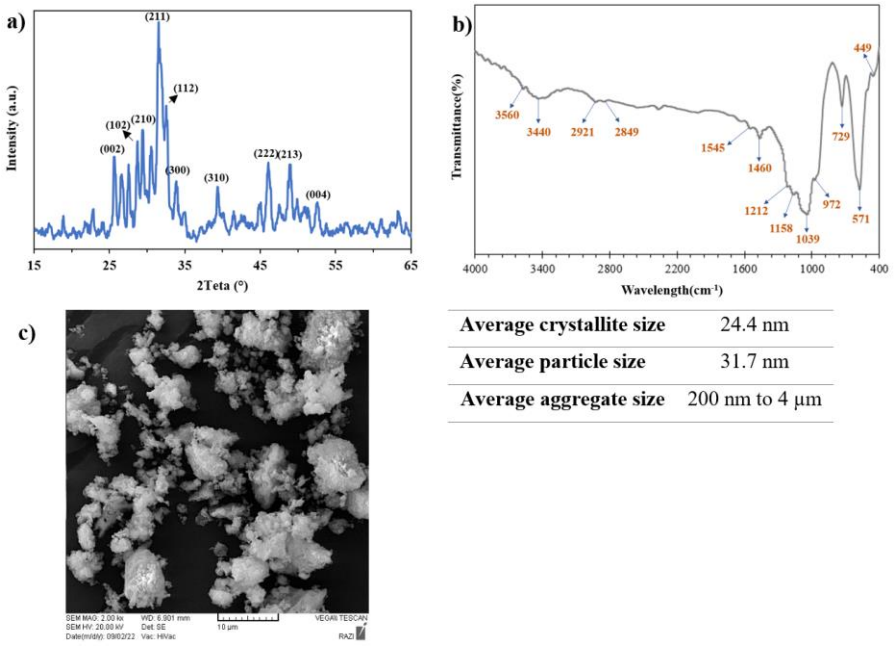

Average crystallite size	24.4 nm
Average particle size	31.7 nm
Average aggregate size	200 nm to 4 μm

Figure 1. XRD pattern, b) FTIR spectrum, and c) the microstructure of npHA synthesized by sol-gel method.

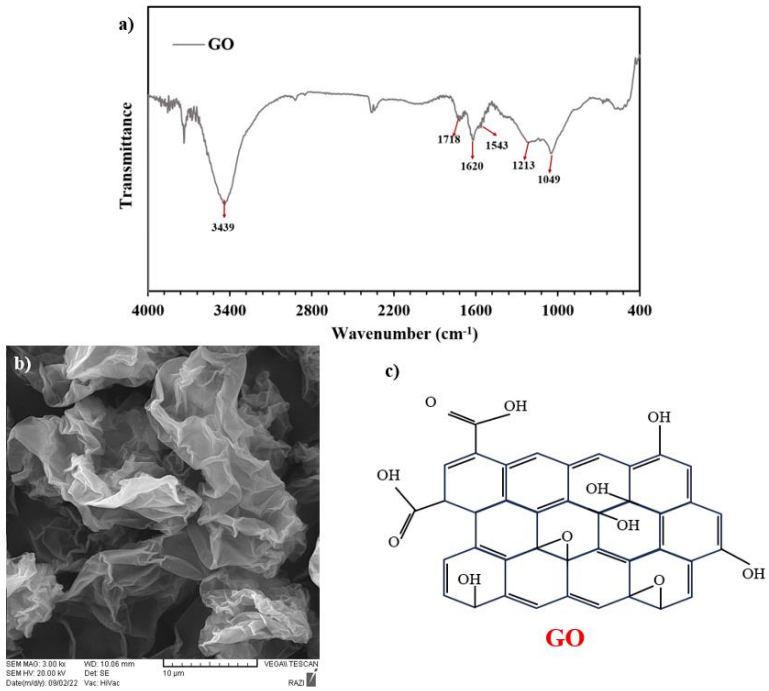

Figure 2. a) FTIR spectrum, b) the SEM images of GO and c) the atomic structures of GO molecules.

3-2- Coating Morphology

Figure 3(a)-(d) shows the microstructure and morphology of the outer surface of the HA-CS-GO coating on the SS316L substrate. A uniform coat is formed over the substrate, as shown in the OM image of the coating surface in Figure 3(a), although some microcracks are observed (pointed to by the red hollow arrow). The SEM images of the coating surface in

Figures 3(b) and (c) show the morphology of the coating microstructure and its constituents. In Figure 3(b), the coating appears relatively uniform; however, at higher magnification (Figure 3(c)), detailed components are discernible. Additionally, the agglomerations of npHA are shown by the blue patterned arrow, which are formed due to the function of CS as a binder phase. The GO sheets are visible in the coating, as indicated by the green patterned arrow in Figure 3(c). According to Figure 3(d), which shows the cross-section of the coated sample, the average coating thickness was measured from at least 10 different positions to be 12.7 ± 2.1 µm.

The GO sheets can be readily covered by hydrogen bonding (Figure 4) to stabilize HA molecules electrostatically (Saadati et al., 2021b). As Figure 4 shows, the CS and HA molecules can bond together by forming connections between Ca^{2+} on HA and the primary and secondary –OH and NH_2 groups of CS (Dantas et al., 2019; Venkatesan & Kim, 2010). Moreover, the electrically charged GO can absorb Ca^{2+} from the molecules of HA and react with CS molecules to form inter- and intra-molecular hydrogen bonding. Accordingly, electrostatic attractions and hydrogen bonding form between GO and HA/CS structures.

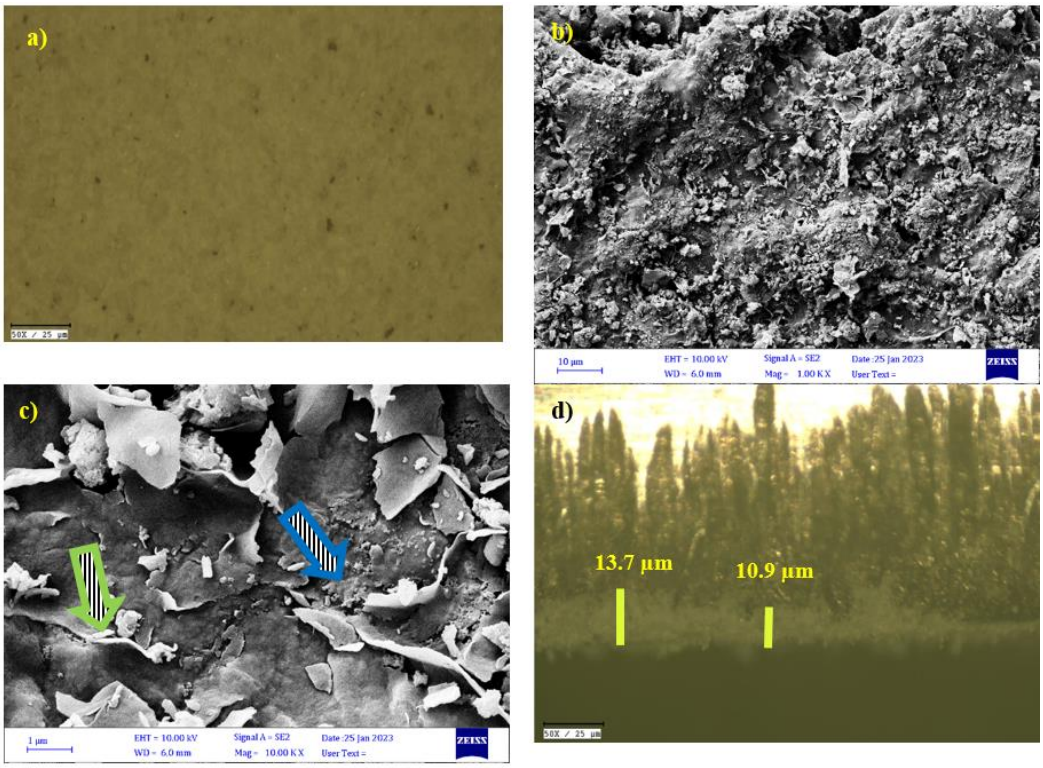

Figure 3. OM images of a) coating surface, and b) coating cross section, and c, and d) SEM images of coting surface. (Yellow and red solid arrows show the sub-micro pores, and GO sheet, respectively. The red hollow, and blue patterned arrows point to the micro crack, and npHA agglomerations, respectively.

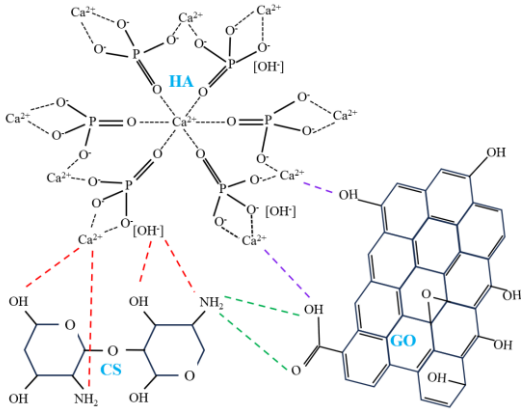

Figure 4. The structure of the GO, HA and CS molecules and their iner-molecular bonds and connections.

3-3-CORROSION BEHAVIOR

In order to evaluate the corrosion behavior of the coating on the corrosion performance, the corrosion properties of the coated SS316L sheet were assessed through potentiodynamic polarization and electrochemical impedance spectroscopy (EIS) analyses in the SBF solution. Figure 5 shows the polarization curves of the substrate and the coated sample, and the electrochemical data for corrosion rate (current density) and corrosion potential, derived from the Tafel extrapolation lines, are presented for comparison. According to the results, the coated sample exhibited lower i_{corr} and higher E_{corr} than the uncoated SS316L sheet. This can be attributed to the very restricted access of the corrosive agents from the electrolyte to the substrate due to the coating. The coating has improved the corrosion resistance. The connection of GO with HA molecules creates a more compact and adhesive structure in the coating microtexture, which enhances corrosion resistance (Arul Xavier Stango & Vijayalakshmi, 2021).

To evaluate the corrosion mechanism and electrochemical features of the coating in the SBF, electrochemical impedance spectroscopy (EIS) analysis was employed. The results of the EIS test, including Nyquist, phase, and Bode plots, are presented for the coated sample in SBF in Figures 6(a) to (c). The Nyquist plot in Figure 6(a) shows a small semicircle at high frequency and a broader semicircle at low frequency, respectively. These semicircles in the Nyquist plot can be related to the reactions at the coating-SBF and the SBF-metal interfaces (Hafedh et al., 2017). Moreover, there are two peaks in the frequency ranges of 10,000 to 100,000 Hz and 0.1 to 10 Hz in the phase plot (Figure 6(b)), which correspond to the two semicircles of the Nyquist plot. The Bode plot in Figure 6(c) confirms the Nyquist and phase results and shows the total resistance value to be 53083 $\Omega.cm^2$. The capacitance of the coating was proposed by estimating the dielectric properties of the material through the equivalent electric circuit (EEC) that was fitted to the experimental EIS data. Accordingly, the experimental data from the EIS analysis were simulated by Zview software modeling, and the obtained EEC is shown in Figure 6(d). The acquired fitting shows excellent correspondence to the EIS data; in Figures 6(a) to (c), the lines and points represent the estimated model and experimental data, respectively. This model includes various elements in the electric circuit, such as the resistances and capacitances of R1, R2, R3, CPE1, and CPE2. The CPE (constant phase element) does not represent an ideal capacitor. This occurs due to the non-parallel double layer and the roughness of the interfaces. R1 represents the electrolyte resistance. R2 and R3 are the resistances of the nanocomposite coating and the charge transfer (double-layer) resistance at the metal/electrolyte interface, respectively. CPE1 and CPE2 correspond to the capacitances of the double layer at the substrate/electrolyte interface and the coating/electrolyte interface, respectively. Figure 6(e) presents the electrochemical parameters obtained from modeling the EIS results and shows the estimated charge transfer resistance at the interface to be 104,607 $\Omega \cdot cm^2$, indicating considerable resistance against progressing corrosion.

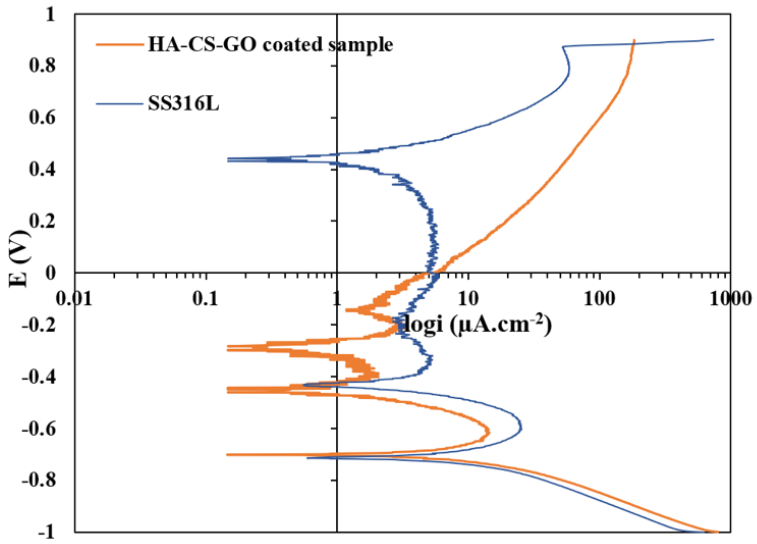

Samples	E_{corr} (V)	I_{corr} (µ.cm^{-2})
SS316LC	-0.714	706
Coated sample (HA-CS-GO)	-0.461	1.4

Figure 5. The polarization curves of E vs logi for the bare substrate and HA-CS -GO coated sample, and the resulted data from the Tafel extrapolation.

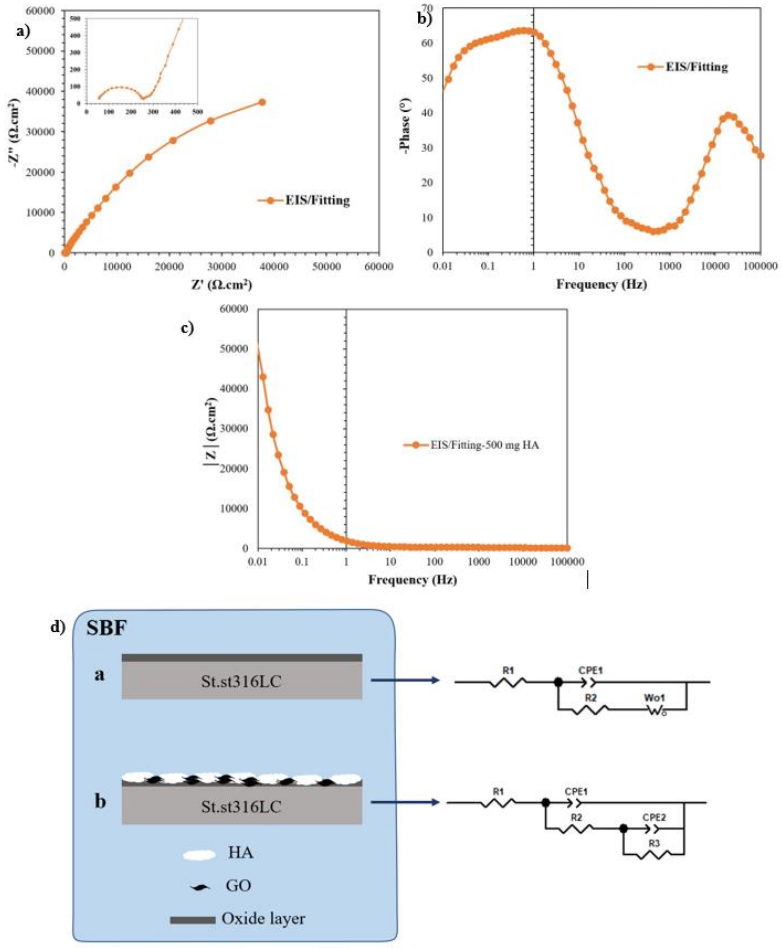

Samples	R1(Ω.cm²)	CPE1 (µF)	R2(Ω.cm²)	CPE2(µF)	R3(Ω.cm²)
Coated sample (HA-CS-GO)	43.82	2.3E-7	226.4	1.6E-4	104607

Figure 6. a) Nyquist, b) phase, and c) Bode plots with the fitted lines of the EEC mathematical model for the coated sample, and d) a schematic simulation of the electrochemical events and its representative EEC model, e) the electrochemical parameters obtained from modeling of the EIS results.

4. CONCLUSION(S)

The nano-composite coating, consisting of npHA, CS, and reduced and functionalized graphene oxide (GO), was applied to an SS316L sheet using the electrophoretic deposition (EPD) method to evaluate the morphology and corrosion performance of the coating in biological environments. The following results were obtained. Additionally, npHA was synthesized by the sol-gel method, and the features of the product were evaluated.

- The particle size and crystallite size of the synthesized HA nanoparticles with spherical morphology were 31.7 nm and 24.4 nm, respectively.
- The properties of GO were examined and confirmed by FTIR spectroscopy and SEM images.
- The microstructure and thickness of the HA-CS-GO nano-composite coating were evaluated by SEM and Optical Microscopy (OM) imaging.
- A uniform HA-CS-GO coating with an average thickness of 12.7 µm was properly deposited onto the SS316L substrate by the EPD method.
- The corrosion behavior of the material before and after deposition was studied by polarization analysis, which confirmed the improved resistance to corrosion due to the coating. The current density for SS316L decreased from 7.6 to 1.4 $\mu A \cdot cm^{-2}$ after coating.
- The compact and adhesive HA-GO-CS coating can act as a barrier against the diffusion of corrosive agents toward the substrate.
- According to the EIS results, the corrosion mechanism for the coated sample was evaluated. No significant sensitivity to local corrosion was detected. The corresponding equivalent circuit with two time constants was simulated, and the dielectric capacitance and resistance values were estimated.
-

ACKNOWLEDGEMENT

Special thanks to Miss Sara Khaleqpasand, very talented materials engineer for her kind assistance in the experiments.

REFERENCES

1. Akram, W., Khan, R., Petrů, M., Amjad, M., Ahmad, K., Yasir, M., Ahmad, S., & Rahimian Koloor, S. S. (2023). Hydroxyapatite coating for control degradation and parametric optimization of pure magnesium: an electrophoretic deposition technique for biodegradable implants. *Journal of Materials Research and Technology*, *26*, 2587–2600. https://doi.org/10.1016/j.jmrt.2023.08.026
2. Al-Gaashani, R., Najjar, A., Zakaria, Y., Mansour, S., & Atieh, M. A. (2019). XPS and structural studies of high quality graphene oxide and reduced graphene oxide prepared by different chemical oxidation methods. *Ceramics International*, *45*(11), 14439–14448. https://doi.org/10.1016/j.ceramint.2019.04.165
3. Arul Xavier Stango, S., & Vijayalakshmi, U. (2021). Electrochemical deposition of HAP/f-MWCNTs and HAP/GO composite layers on 316L SS implant with excellent corrosion resistance performance. *Materials Letters*, *304*(March), 130666. https://doi.org/10.1016/j.matlet.2021.130666
4. Asadipour, K., Nezafati, N., Nourbakhsh, M. S., Hafezi-Ardakani, M., & Bohlooli, S. (2019). Characterization and biological properties of a novel synthesized silicon-substituted hydroxyapatite derived from eggshell. *The International Journal of Artificial Organs*, *42*(2), 95–108. https://doi.org/10.1177/0391398818806159
5. Asgar, H., Deen, K. M., Rahman, Z. U., Shah, U. H., Raza, M. A., & Haider, W. (2019). Functionalized graphene oxide coating on Ti6Al4V alloy for improved biocompatibility and corrosion resistance. *Materials Science and Engineering C*, *94*(October 2018), 920–928. https://doi.org/10.1016/j.msec.2018.10.046
6. Askarnia, R., Fardi, S. R., Sobhani, M., & Staji, H. (2021). Ternary hydroxyapatite/chitosan/graphene oxide composite coating on AZ91D magnesium alloy by electrophoretic deposition. *Ceramics International*, *47*(19), 27071–27081. https://doi.org/10.1016/j.ceramint.2021.06.120
7. Baslayici, S., Bugdayci, M., Benzesik, K., Yucel, O., & Acma, M. E. (2022). Corrosion behavior of hydroxyapatite coated AZ31 and AZ91 Mg alloys by electrostatic spray coating. *International Journal of Materials Research*, *113*(2), 93–100. https://doi.org/10.1515/ijmr-2021-8310
8. Chen, J., Wang, Y., Chen, X., Ren, L., Lai, C., He, W., & Zhang, Q. (2011). A simple sol-gel technique for synthesis of nanostructured hydroxyapatite, tricalcium phosphate and biphasic powders. *Materials Letters*, *65*(12), 1923–1926. https://doi.org/10.1016/j.matlet.2011.03.076
9. Choi, G., Choi, A. H., Evans, L. A., Akyol, S., & Ben-Nissan, B. (2020). A review: Recent advances in sol-gel-derived hydroxyapatite nanocoatings for clinical applications. *Journal of the American Ceramic Society*, *103*(10), 5442–5453. https://doi.org/10.1111/jace.17118
10. Dantas, M. J. L., Santos, B. F. F., Tavarez, A. A., Maciel, M. A., Lucena, B. M., Fook, M. V., & Silva, S. M. (2019). Physical and In Vitro Dexamethasone Release Properties of Chitosan / Hydroxyapatite Beads. *Molecules*, *24*, 1–20. https://doi.org/10.3390/molecules24244510
11. Das, S. S., & Chakraborti, P. (2021). Tribological performances of a novel biopolymeric material HD-HA for hip joint implants. *Emerging Materials Research*, *10*(3), 329–340. https://doi.org/10.1680/jemmr.20.00005
12. Dhinasekaran, D., Kaliaraj, G. S., Jagannathan, M., Rajendran, A. R., Prakasarao, A., Ganesan, S., & Subramanian, B. (2021). Pulsed laser deposition of nanostructured bioactive glass and hydroxyapatite coatings: Microstructural and electrochemical characterization. *Materials Science and Engineering: C*, *130*, 112459. https://doi.org/10.1016/j.msec.2021.112459
13. Dvorsky, D., Gambardella, A., Kubasek, J., Berni, M., & Vojtech, D. (2020). Ultrathin hydroxyapatite coating on pure magnesium substrate prepared by pulsed electron ablation technique. *Materials and Corrosion*, *71*(11), 1794–1801. https://doi.org/10.1002/maco.202011721
14. Eliaz, N. (2019). Corrosion of metallic biomaterials: A review. *Materials*, *12*(3). https://doi.org/10.3390/ma12030407
15. Fardi, S. R., khorsand, H., Askarnia, R., Pardehkhorram, R., & Adabifiroozjaei, E. (2020). Improvement of biomedical functionality of titanium by ultrasound-assisted electrophoretic deposition of hydroxyapatite-graphene oxide nanocomposites. *Ceramics International*, *46*(11, Part A), 18297–18307. https://doi.org/10.1016/j.ceramint.2020.05.049
16. Gheisari, H., Karamian, E., & Abdellahi, M. (2015). A novel hydroxyapatite -Hardystonite nanocomposite ceramic. *Ceramics International*, *41*(4), 5967–5975. https://doi.org/10.1016/j.ceramint.2015.01.033
17. Guo, Y., Wang, L., & Sun, X. (2023). GO-Al2O3 nanohybrids to enhance the anticorrosion performance of chemically bonded ceramic coatings. *Materials and Corrosion*, *74*(2), 320–328. https://doi.org/10.1002/maco.202213271
18. Hafedh, D., Kaouther, K., & Ahmed, B. C. L. (2017). Multi-property improvement of TiO2-WO3 mixed oxide films deposited on 316L stainless steel by electrophoretic method. *Surface and Coatings Technology*, *326*, 45–52. https://doi.org/10.1016/j.surfcoat.2017.07.041
19. Harun, W. S. W., Asri, R. I. M., Alias, J., Zulkifli, F. H., Kadirgama, K., Ghani, S. A. C., & Shariffuddin, J. H. M. (2018). A comprehensive review of hydroxyapatite-based coatings adhesion on metallic biomaterials. *Ceramics International*, *44*(2), 1250–1268. https://doi.org/10.1016/j.ceramint.2017.10.162
20. Hudecki, A., Kiryczyński, G., & Łos, M. J. (2018). Biomaterials, definition, overview. *Stem Cells and Biomaterials for Regenerative Medicine*, *ii*, 85–98. https://doi.org/10.1016/B978-0-12-812258-7.00007-1
21. Jeyaseelan, A., Ghfar, A. A., Naushad, M., & Viswanathan, N. (2021). Design and synthesis of amine functionalized graphene oxide for enhanced fluoride removal. *Journal of Environmental Chemical Engineering*, *9*(4), 105384. https://doi.org/10.1016/j.jece.2021.105384
22. Kesmez, Ö. (2020). Preparation of anti-bacterial biocomposite nanofibers fabricated by electrospinning method. *Journal of the Turkish Chemical Society, Section A: Chemistry*, *7*(1), 125–142. https://doi.org/10.18596/jotcsa.590621
23. Khalid, M., Mujahid, M., Khan, A. N., & Rawat, R. S. (2013). Dip Coating of Nano Hydroxyapatite on Titanium Alloy with Plasma Assisted γ-Alumina Buffer Layer: A Novel Coating Approach. *Journal of Materials Science and Technology*, *29*(6), 557–564. https://doi.org/10.1016/j.jmst.2013.02.003
24. Kuo, P. H., & Du, J. (2022). Effect of boron oxide on mechanical and thermal properties of bioactive glass coatings for biomedical applications. *Journal of the American Ceramic Society*, *105*(6), 3986–4008. https://doi.org/10.1111/jace.18391
25. Kusrini, E., Oktavianto, F., Usman, A., Mawarni, D. P., & Alhamid, M. I. (2020). Synthesis, characterization, and performance of graphene oxide and phosphorylated graphene oxide as additive in water-based drilling fluids. *Applied Surface Science*, *506*, 145005. https://doi.org/10.1016/j.apsusc.2019.145005

26. Liao, M., Shi, Y., Chen, E., Shou, Y., Dai, D., Xian, W., Ren, B., Xiao, S., & Cheng, L. (2022). The Bio-Aging of Biofilms on Behalf of Various Oral Status on Different Titanium Implant Materials. *International Journal of Molecular Sciences*, *24*(1), 332. https://doi.org/10.3390/ijms24010332

27. Logesh, M., Marimuthu, A., Ferreira, J. M. F., Ramakrishnan, P., & Ballamurugan, A. M. (2022). Evaluation of the protective nature of GO–BCP nanocomposite coatings on 316L SS in artificial body fluid. *Journal of the American Ceramic Society*, *June*, 3843–3852. https://doi.org/10.1111/jace.18975

28. Modolon, H. B., Inocente, J., Bernardin, A. M., Klegues Montedo, O. R., & Arcaro, S. (2021a). Nanostructured biological hydroxyapatite from Tilapia bone: A pathway to control crystallite size and crystallinity. *Ceramics International*, *47*(19), 27685–27693. https://doi.org/10.1016/j.ceramint.2021.06.193

29. Modolon, H. B., Inocente, J., Bernardin, A. M., Klegues Montedo, O. R., & Arcaro, S. (2021b). Nanostructured biological hydroxyapatite from Tilapia bone: A pathway to control crystallite size and crystallinity. *Ceramics International*, *47*(19), 27685–27693. https://doi.org/10.1016/j.ceramint.2021.06.193

30. Monai, N., Kuwabara, A., Kawanishi, N., Ozawa, R., Adachi, T., Tsunoi, S., Inoue, M., Saita, M., Hayakawa, T., & Hoshi, N. (2023). Effect of UV Photofunctionalization of HA/TiO2 Coated Implants Prepared by Dual-Target Sputtering on Bone-Implant Integration. *Journal of Hard Tissue Biology*, *32*(2), 99–104 https://doi.org/10.2485/jhtb.32.99

31. Mujahid, M., Sarfraz, S., & Amin, S. (2015). On the Formation of Hydroxyapatite Nano Crystals Prepared Using Cationic Surfactant. *Materials Research*, *18*(3), 468–472. http://dx.doi.org/10.1590/1516-1439.298014

32. Naderi, M., & Nadri, S. (2022). Synergistic effect of miR-9 overexpression and electrical induction on differentiation of conjunctiva mesenchymal stem cells into photoreceptor-like cells. *The International Journal of Artificial Organs*, *45*(7), 623–630. https://doi.org/10.1177/03913988221103285

33. Nair, S., Kumar, V., Kumar, R., Jain, V. K., & Nagpal, S. (2022). Electrostatic graphene oxide-based biosensor for rapid direct detection of E. coli. *International Journal of Materials Research*, *113*(6), 560–568. https://doi.org/10.1515/ijmr-2021-8288

34. Onoki, T., & Hashida, T. (2006). New method for hydroxyapatite coating of titanium by the hydrothermal hot isostatic pressing technique. *Surface and Coatings Technology*, *200*(24), 6801–6807. https://doi.org/10.1016/j.surfcoat.2005.10.016

35. Pan, X., You, C., Wu, P., Wang, X., & Han, C. (2023). The optimization of PLGA knitted mesh reinforced-collagen/chitosan scaffold for the healing of full-thickness skin defects. *Journal of Biomedical Materials Research - Part B Applied Biomaterials*, *111*(4), 763–774. https://doi.org/10.1002/jbm.b.35187

36. Perju, M.-C., Nejneru, C., Vizureanu, P., Aelenei, A.-A., Sandu, A. V., Sachelarie, L., & Nabiałek, M. (2022). Some Aspects Concerning Titanium Coverage with Hydroxyapatite. *Archives of Metallurgy and Materials*, *67*. https://doi.org/10.24425/amm.2022.137785

37. Prasanna, A. P. S., & Venkatasubbu, G. D. (2018). Sustained release of amoxicillin from hydroxyapatite nanocomposite for bone infections. *Progress in Biomaterials*, *7*(4), 289–296. https://doi.org/10.1007/s40204-018-0103-4

38. Priyam, A., Das, R. K., Schultz, A., & Singh, P. P. (2019). A new method for biological synthesis of agriculturally relevant nanohydroxyapatite with elucidated efects on soil bacteria. *Scientific Reports*, *9*, 5083–5097. https://doi.org/doi: 10.1038/s41598-019-51514-0

39. Saadati, A., Khiarak, B. N., Zahraei, A. A., Nourbakhsh, A., & Mohammadzadeh, H. (2021a). Electrochemical characterization of electrophoretically deposited hydroxyapatite/chitosan/graphene oxide composite coating on Mg substrate. *Surfaces and Interfaces*, *25*(June), 101290. https://doi.org/10.1016/j.surfin.2021.101290

40. Saadati, A., Khiarak, B. N., Zahraei, A. A., Nourbakhsh, A., & Mohammadzadeh, H. (2021b). Electrochemical characterization of Electrophoretically deposited Hydroxyapatite/Chitosan/Graphene Oxide composite coating on Mg substrate. *Surfaces and Interfaces*, *25*(December 2020), 101290. https://doi.org/10.1016/j.surfin.2021.101290

41. Sahoo, P. C., Dash, T., Mallick, S. C., & Biswal, S. K. (2023). Reduced graphene oxide synthesis by dry planetary ball milling followed by arc plasma treatment of high pure graphite. *International Journal of Materials Research*, *114*(4–5), 299–307. https://doi.org/10.1515/ijmr-2022-0071

42. Shanmugapriya, Sivamaran, V., Padma Rao, A., Senthil Kumar, P., Selvamani, S. T., & Mandal, T. K. (2022). Sol–gel derived Al2O3/Gr/HAP nanocomposite coatings on Ti–6Al–4V alloy for enhancing tribo-mech properties and antibacterial activity for bone implants. *Applied Physics A*, *128*(8), 635. https://doi.org/10.1007/s00339-022-05784-7

43. Shi, Y. Y., Li, M., Liu, Q., Jia, Z. J., Xu, X. C., Cheng, Y., & Zheng, Y. F. (2016). Electrophoretic deposition of graphene oxide reinforced chitosan–hydroxyapatite nanocomposite coatings on Ti substrate. *Journal of Materials Science: Materials in Medicine*, *27*(3), 1–13. https://doi.org/10.1007/s10856-015-5634-9

44. Sorkhi, L., Farrokhi-Rad, M., & Shahrabi, T. (2019). Electrophoretic Deposition of Hydroxyapatite–Chitosan–Titania on Stainless Steel 316 L. *Surfaces*, *2*(3), 458–467. https://doi.org/10.3390/surfaces2030034

45. Staneva, A. D., Dimitrov, D. K., Gospodinova, D. N., & Vladkova, T. G. (2021). Antibiofouling activity of graphene materials and graphene-based antimicrobial coatings. *Microorganisms*, *9*(9), 1–20. https://doi.org/10.3390/microorganisms9091839

46. Vahabzadeh, S., Roy, M., Bandyopadhyay, A., & Bose, S. (2015). Phase stability and biological property evaluation of plasma sprayed hydroxyapatite coatings for orthopedic and dental applications. *Acta Biomaterialia*, *17*, 47–55. https://doi.org/10.1016/j.actbio.2015.01.022

47. Venkatesan, J., & Kim, S. K. (2010). Chitosan composites for bone tissue engineering - An overview. *Marine Drugs*, *8*(8), 2252–2266. https://doi.org/10.3390/md8082252

48. Verma, P. K., Mehta, A., Vasudev, H., & Kumar, V. (2023). Performance of thermal spray coated metallic materials for bio-implant applications. *Surface Review and Letters*, 2340012. https://doi.org/10.1142/S0218625X23400127

49. Wadood, A. (2021). *Ag – Sr doped mesoporous bioactive glass nanoparticles loaded chitosan / gelatin coating for orthopedic implants*. *December 2020*, 544–562. https://doi.org/10.1111/ijac.13702

50. Zahra, I., Sun, Y., Anjum, Z., Azadani, M. N., & Tajmal, A. (2023). Effect of environments on the tribological behaviour of pure and graphene coated nickel against stainless steel counterpart. *International Journal of Surface Science and Engineering*, *17*(3), 231–247. https://doi.org/10.1504/IJSURFSE.2023.134788

51. Zhang, W., Xu, H., Xie, F., Ma, X., Niu, B., Chen, M., Zhang, H., Zhang, Y., & Long, D. (2022). General synthesis of ultrafine metal oxide/reduced graphene oxide nanocomposites for ultrahigh-flux nanofiltration membrane. *Nature Communications*, *13*(1), 1–10. https://doi.org/10.1038/s41467-022-28180-4